Progress Towards an Open-Source, Low-Cost Ultrasound Computed Tomography Research System

Morgan J. Roberts[1], Eleanor Martin[1], Ben T. Cox[1], and Bradley E. Treeby[1]

[1]*Department of Medical Physics and Biomedical Engineering, University College London, London, UK, E-mail: morgan.roberts.18@ucl.ac.uk*

Abstract

Ultrasound Computed Tomography (UCT) systems are typically custom-built, and the high cost and long lead time can be a significant barrier to research groups becoming active in the field. This work details progress towards FlexUCT: a design framework for a low-cost benchtop UCT system that will allow novel data acquisition protocols and reconstruction algorithms to be tested on a physical system, thereby facilitating progress towards fast and accurate UCT. The design, assembly and testing of 4-element prototypes are described. Field scans of the prototypes have been performed to characterise the beamwidth, element radiation pattern and acoustic cross talk, and the pulse echo behaviour was evaluated.

Keywords: Ultrasound Computed Tomography, Low Cost Hardware, Open Source, US Transducer

1 Introduction

Ultrasound Computed Tomography (UCT) is a biomedical imaging technique that involves sending pulses of ultrasound into the tissue, often the breast, from different angles, and measuring the reflected and transmitted pulses with an array of detectors [1]. UCT has the advantages of being non-ionising, operator-independent, and pain-free since it requires no breast compression [2].

However, for researchers seeking to start working on UCT the barrier to entry is high, because to properly test novel data acquisition protocols and image reconstruction methods, custom hardware is required in order to have sufficient control over the experimental setup to meet the specific research needs, and custom systems can be prohibitively expensive and

often have a long lead time. Lowering this barrier will increase participation in the field, which is likely to result in more and faster progress towards improved image reconstruction algorithms and data acquisition protocols.

This paper describes the initial developmental stages of FlexUCT, an open source design framework for a benchtop UCT research system. The framework uses a toolbox of flexible, low-cost manufacturing techniques which allow the user to choose their own values for key design parameters, such as aperture size and element dimensions, without affecting the assembly processes. The framework is designed to have simple user requirements for manufacture, requiring only standard workshop hand tools, a mill and a 3-D printer, which are commonly available in most research institutions. Our future goal is to distribute the complete specification needed to build a custom UCT research system, including parametric CAD models, 3D-printing design files, Gerber files for PCB manufacture, a bill of materials and a full assembly procedure. Here, we present the design, assembly, and evaluation of the first FlexUCT prototypes.

2   Design and Modelling

2.1   Aperture Configuration

To develop flexible manufacturing techniques, our approach was to first design a typical full-aperture UCT ring, but to build this in smaller 4-element segments. This allows rapid iteration with lower material costs, and also ensures that the manufacturing techniques can be used to realise modular apertures as well as fixed apertures. The KIT and MUBI UCT systems demonstrate that multiple modular segments can be assembled to realise 2D [3] and 3D [4] apertures, which could provide greater flexibility to FlexUCT users by allowing changes to the aperture configuration without manufacturing new hardware, and by allowing easy replacement of faulty elements.

The CURE prototype [5] has previously shown that 256 transducers are sufficient for basic UCT imaging in a 2D ring configuration, and since 3D apertures require an order of magnitude more transducers, meaning complicated and expensive multiplexing would have to be used, it was decided to use a 2D ring array configuration with 256 equispaced transducers as shown in Figure 1. This matches the number of available transmit/receive channels for the ULA-OP, UARP, and Verasonics Vantage systems, which are three commonly available platforms for ultrasound data acquisition [6]. In principle the system could be rotated to obtain measurements at a finer angular spacing. A ring diameter of 220mm was chosen, based on an assessment of breast diameter from 200 women in America showing that a ring of this size would accommodate 95% of the population [7], which is shown in Figure 1 with the PZT element dimensions.
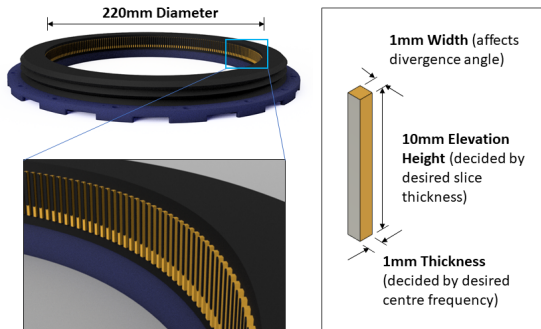
Figure 1: Left: Full-aperture UCT ring, designed with 256 equispaced transducer elements embedded in a common backing layer, and with a diameter of 220 mm. Right: A single PZT element defined by the key dimensions shown, with solid pattern electrodes.

2.2 PZT Element Dimensions

The centre frequency of a PZT element is dominated by its half-wave resonance, which is controlled by its thickness when driven as a width expander [8], and should be as high as possible for good resolution, but low enough to prevent excessive absorption. For a plane wave travelling in the $+z$ direction, the solution to the lossy Helmholtz equation is $p = P_0 e^{-\alpha z} e^{j(\omega t - kz)}$ [9], where p is the acoustic pressure, ω is the angular frequency, k is the wavenumber, and t is time. This shows that as a wave propagates through an absorbing medium over a distance z, the plane wave amplitude P_0 decays according to $\exp(-\alpha z)$. In tissue, the frequency dependent acoustic absorption coefficient $\alpha(f)$ follows a power law relationship described by $\alpha(f) = \alpha_0 |f|^y$, where $\alpha_0 = 0.75$ dB.MHz^{-y}.cm^{-1} and $y = 1.5$ for breast tissue [8]. Using these material properties, a mean breast diameter of $z = 140$ mm, and an assumed noise floor of 5%, a centre frequency of $f = 2$ MHz results in an acceptable decay, which corresponds to a PZT element thickness of 1 mm with a sound speed of 4010 m.s^{-1} [10].

The elevation height of an element affects the beamwidth and therefore the image slice thickness. To avoid variations in the effect of volume averaging, the slice thickness would ideally be constant over the imaged region [2]. To choose an appropriate elevation height, simulations were performed using the acoustic field propagator from the k-Wave toolbox in MATLAB [11] [12]. For a range of element sizes, the transmitted field in the elevation plane was computed at a frequency of 2 MHz for a ring of diameter 220 mm. As the receive sensitivity will have the same spatial dependence, the transmit-receive sensitivity was found by multiplying the transmitted field with a copy of itself flipped about the central point of the array. The resulting transmit-receive sensitivity is shown in Figure 2. The full-width-half-maximum of the beam at the centre of the array was then extracted. As the element elevation height increases, the beamwidth at the centre decreases as expected, but beyond the 10 mm element size, the improvement in beamwidth comes at the expense of a much wider and longer near field which could affect the image reconstruction at the edges of phantoms larger

than 100 mm. An element elevation height of 10 mm was chosen as a good balance between slice thickness at the centre of the array and slice uniformity across the region of interest.

For UCT, the elements would ideally be as narrow as possible so that they are very diverging in the scan plane and achieve full coverage of the breast. However, it is important for this system to be easily and repeatably assembled by hand, so the element width was chosen to be 1 mm, so that the electrode area is large enough to easily terminate signal leads by hand-soldering. The final element dimensions can be seen in Figure 1.
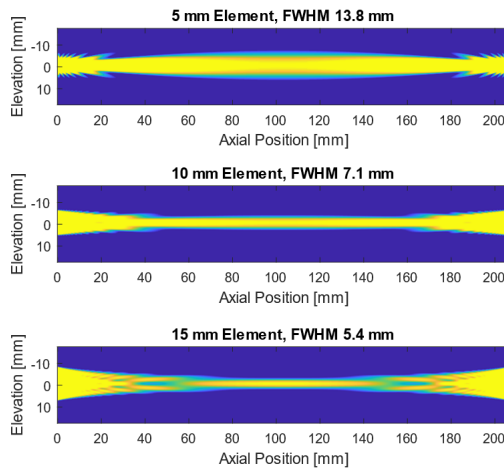

Figure 2: Elevation plane transmit-receive sensitivity plots for rectangular bar elements driven at 2 MHz, for a range of elevation heights. Pressure is displayed on a logarithmic scale, referenced to the maximum pressure at the centre of the ring, and thresholded to a 6 dB range. The element width was 1 mm for all simulations.

2.3   Acoustic Properties of Tungsten-Epoxy Composites

To fabricate matching and backing layers, tungsten particles can be embedded in an epoxy resin polymer matrix to form a 0-3 composite. A study was performed to establish the relationship between tungsten-epoxy weight ratio and the acoustic properties of the resulting composite under a specific set of repeatable conditions, since previous work has only been completed at much higher frequencies [13], and work by Grewe et al. suggests that the relationship is affected by tungsten particle size and mixing techniques [14].

Tungsten-epoxy samples were manufactured with tungsten weight ratios ranging from 72.5% to 95%. To calculate the characteristic impedance of the samples, their sound speed was measured in deionised water using the through-transmission substitution method [15], and their density was calculated using a simplified hydrostatic weighing method [16]. Figure 3 shows the measured sound speed and characteristic impedance, alongside the predicted acoustic properties of the samples calculated using the Devaney model, which gives expressions for

the effective bulk and shear moduli of a random distribution of elastic spheres embedded in an elastic matrix, using multiple scattering theory [17]. The shape of the predicted sound speed profile is qualitatively similar to the experimental data, showing a sound speed minimum at a tungsten weight ratio of 87.5%, but the model does not match the data quantitatively since it doesn't account for absorption, and since it also depends heavily on the values used for the bulk and shear moduli of the epoxy matrix and tungsten particles. The experimental results are important because they can be interpolated to manufacture tungsten-epoxy matching and backing layers with a desired characteristic impedance.
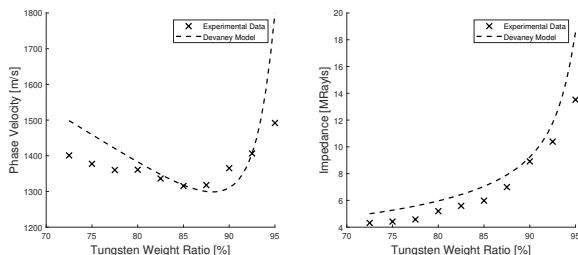

Figure 3: Experimental data showing the relationship between the tungsten weight ratio of a tungsten-epoxy composite and its phase velocity and characteristic impedance at 2 MHz. The acoustic properties from the Devaney model [17] are also shown.

2.4 CAD Design

The prototype transducers were designed in CAD software, shown in Figure 4. PZT elements with a single tungsten-epoxy matching layer on their front face are embedded in a 12 mm tungsten-epoxy backing layer, which is mounted on an acrylic cable-guide plate, which has holes to align the individual signal leads with the rear electrode on each element. The individual signal leads combine into a flat ribbon cable, which is secured to the cable-guide plate with a strain relief clip. A common ground electrode connects to a $1.5{\times}1$ mm unmatched area on the front electrode of each PZT element.

3 Assembly Methods

3.1 Quarter-Wave Matching Layer

For a layer of tungsten-epoxy used to match PZT with impedance $Z_p = 30.5$ MRayl to water with impedance $Z_w = 1.5$ MRayl, the impedance of the matching layer should be $Z_l = \sqrt{30.5 \times 1.5} = 6.76$ MRayl. This can be achieved by using a tungsten weight ratio of $W_T = 86.9\%$, which has a sound speed of 1317 m.s^{-1}, meaning that the target quarter wave matching layer thickness is $\lambda/4 = 165$ μm at 2 MHz.
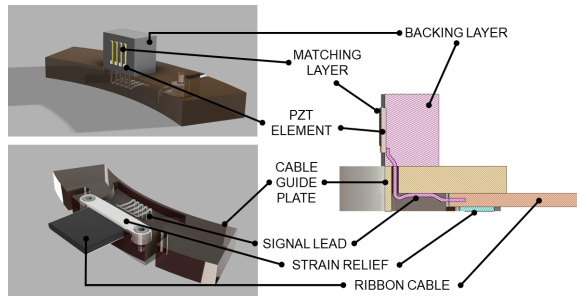
Figure 4: CAD rendering of prototypes, with the key components labelled. The right hand diagram is an elevation plane cross section down the centre of one of the PZT elements. Note that the common ground electrode on the front face of the PZT elements is not shown.

Previous low cost transducers have used a 3D-printed mould to control the matching layer thickness by supporting the PZT element on 'standoffs' which are exactly $\lambda/4$ [18]. Preliminary work showed that as frequency increases, matching layer thicknesses becomes less repeatable, because the required thickness approaches the layer height of the 3-D printed standoffs, meaning that the technique is not suitably flexible. Alternatively, it has been shown that metal foils can be used as a stencil to deposit solder pastes with a uniform and controlled geometry for circuit board assembly [19], and that blade coating can be used for depositing thin films with a controllable thickness [20].

In order to replicate a hybrid of these techniques, a stencil was manufactured by using a 1 mm end mill to create 1×8.5 mm slots in 0.2 mm steel shim stock. A jig was milled from acrylic with 1 mm slots to receive the PZT elements and hold their top face flush with the surface. The stencil was placed on top of the elements using registration pins, and the tungsten-epoxy composite was spread over the slots using a blade. On removal of the stencil, the tungsten-epoxy composite covered the PZT element with a controlled geometry, and was left to cure at room temperature. This process is shown in Figure 5.

To test the repeatability of the technique, 45 samples were deposited and the thickness was measured with digital callipers. The mean sample thickness was 150.9 μm, and the standard deviation was 15.4 μm, placing the 165 μm target thickness within one standard deviation of the mean. Future work will be done to establish the relationship between the stencil thickness and the final cured thickness of the deposited layers, but this preliminary study suggests that the proposed method can deposit matching layers repeatably with a suitable thickness.

3.2 PZT Element Alignment Mould

It is important that the front faces of the elements are aligned tangent to the ring geometry. If they are skewed, then the breast may not be homogeneously insonified, which can cause artefacts [21]. Moulds with slots to retain each element were manufactured from polyvinyl
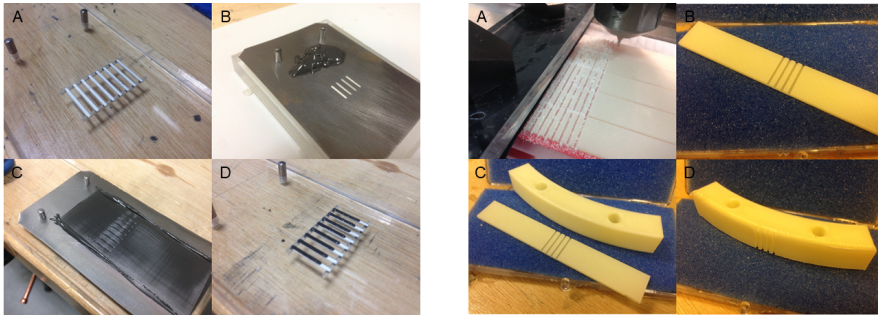
Figure 5: Left: Proposed method used to deposit matching layers. A) PZT Elements are placed into slots in a jig, with their top face flush with the surface. B) A steel stencil is placed on top, and the tungsten-epoxy composite is added. C) The tungsten-epoxy composite is spread over the stencil with a scraper. D) The stencil is removed. Right: Proposed method to manufacture an alignment mould. A) $1 \times 1 \times 13$ mm slots are milled into a strip of 1.5 mm PVA. B) The resulting PVA alignment strip. C) Strip and 3D-printed alignment form before bending. D) The PVA alignment strip is bent and welded onto the alignment form.

alcohol (PVA) in order to align the PZT elements relative to one another. PVA is a water soluble polymer and can easily be removed without damaging the elements by dissolving the moulds. Kerfs were milled from a 3D-printed flat PVA strip, which was then bent and welded to a 3D printed PVA form, shown in Figure 5. The benefit of using milled slots is that the internal corners are much sharper than those achieved using 3D-printing alone, allowing a much tighter fit to be achieved. To test the PZT element orientation accuracy when using milled slots rather than 3D-printed slots, both methods were used to prepare a 4-element sample, and a microCT scan was performed on each using a XT H 225 scanner (Nikon). A slice was taken through the CT image to show the cross sections of the PZT elements, which can be seen compared to microscope photographs of the samples in Figure 6. This shows that the element alignment achieved using milled slots is more uniform than that achieved using 3D-printing alone.
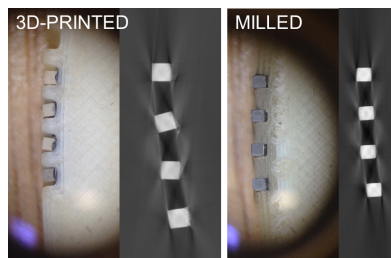

Figure 6: Analysis of the PZT element orientation using microscope photographs (Left) and microCT scans (Right). Two samples were investigated that use different assembly methods to create slots that the PZT elements are placed in. The 3D-printed slots are shown on the left, and the milled slots are shown on the right.

3.3 Further Assembly

Once the deposited matching layers had cured, the PZT elements were fixed in the alignment moulds using a water soluble PVA glue. The flat ribbon cable was then fixed into place with a 3D-printed PLA strain relief clip, and the individual signal leads were distributed through the holes in the cable guide plate, shown in Figure 7. The leads were then soldered to the element electrodes.

A mould for curing the backing layer was 3D-printed from PVA filament. The backing layer mould, cable guide plate, and alignment mould were then all bolted down to a rigid base plate, shown in Figure 7. A tungsten-epoxy composite with a tungsten weight ratio of 92.5% was mixed thoroughly, pushed into the backing layer mould, and allowed to cure at room temperature, bonding directly onto both the rear electrode of the PZT and the cable guide plate, whilst encapsulating the signal leads. A weight ratio of 92.5% is the highest impedance composition available using hand mixing, since beyond this high pressures and temperatures are required to bind the composite together [22]. This was chosen in order to investigate whether the resulting sensitivity is high enough for use in UCT.
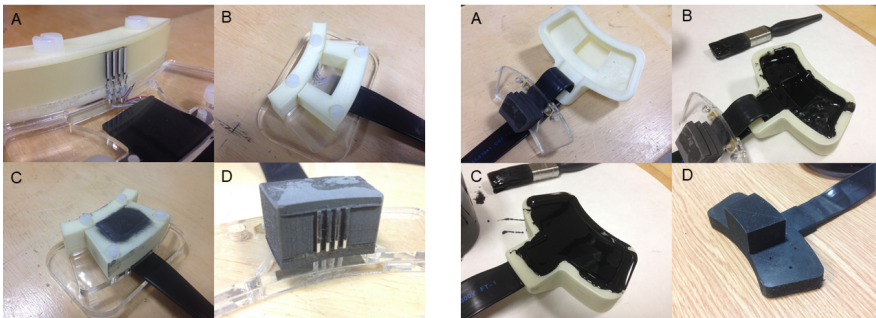

Figure 7: Left: Casting the backing layer. A) Elements are placed in alignment moulds and leads are soldered onto electrodes. B) Backing layer mould fixed into place. C) Tungsten-epoxy backing layer pressed into mould. D) PVA moulds dissolved, leaving elements embedded in backing layer. Right: Coating the transducer. A) Flat ribbon cable threaded through a slot in the coating mould. B) Mould coated with Aptflex F7. C) Transducer placed in the mould and filled up with Aptflex before leaving to cure. D) Finished second generation prototype after PVA mould has been dissolved away.

The PVA moulds were all removed by dissolving them in warm water. In order to waterproof the transducers and to insulate them electrically, a two-component polyurethane coating with an acoustic impedance of 1.5 MRayl was used (Aptflex F7, Precision Acoustics) to minimise the pressure reflection coefficient at the coating-water boundary, preventing internal reverberations within the coating layer. A 3D-printed PVA mould was used to create a coating layer with a consistent thickness, which was again removed by dissolving in water. One of the finished transducers can be seen in Figure 7.

4   Experimental Evaluation

4.1   Field Scan Procedure

Field scans were performed on the prototypes to investigate the pressure distribution on the front of the elements and the beam orientation in the scan plane for each element. Measurements were taken in a tank of deionised water using an X-Y stepper motor positioning system (Precision Acoustics), and the water temperature was monitored using a J-type thermocouple (National Instruments). The transducer was directly connected via a custom 3D-printed backshell to the Vantage-256 (Verasonics), with no electrical impedance matching, and all four channels were driven by a 3 cycle tri-state pulse with a frequency of 2 MHz and an amplitude of 30 V. Signals were acquired at a sampling frequency of 0.2 GHz using a calibrated 200 μm needle hydrophone (Precision Acoustics) connected to an InfiniiVision DSOX3024A digital oscilloscope (Keysight) via a submersible preamplifier and DC coupler (Precision Acoustics) in a 170×170 scanning grid located 27 mm from the transducer surface, with a uniform point spacing of 0.3 mm. The voltage signals were deconvolved using the hydrophone response to give the pressure time series in the measurement plane, which were bandpass filtered. A Tukey window was applied, and the 3D volume of the maximum pressure in the field was calculating by backprojecting using the angular spectrum method [23].

4.2   Elevation Plane Beam Orientation Analysis

To evaluate the orientation of the beams in the elevation plane of the pressure field, the scanning procedure was repeated four times, successively driving each element in isolation. The beam orientation was calculated for each element by drawing a line between the locations of the maximum pressure at two points in the far field, and calculating the angle between this line and the horizontal. This can be seen in Figure 8, which shows the pressure on a logarithmic scale. Although there is a common downwards skew due to misalignment of the scan plane with the transducer, the standard deviation of the beam angles is $\sigma = 0.57°$, which corresponds to a 1.1 mm vertical deviation over a horizontal distance of 110 mm to the centre of the ring. This is sufficiently small to suggest that the milled alignment strip is a suitable low-cost method for aligning the PZT elements relative to one another with high repeatability. The measured beamwidth at the centre of the ring is 9.5 mm, which is slightly greater than the 7.1 mm predicted from the k-Wave simulations, which suggests that the effective element elevation height is smaller than 10 mm.
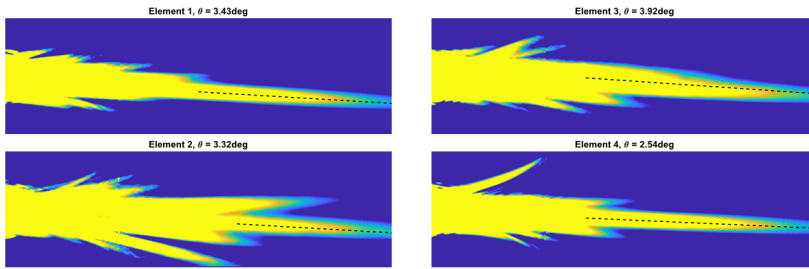
Figure 8: Elevation beam pattern for each of the elements. The centreline of the beam in the far field has been estimated, and the angle of the centreline to the horizontal has been calculated. Pressure is displayed on a logarithmic scale, referenced to a point on the beam axis in the far field, and thresholded to a 6 dB range.

4.3   Element Radiation Pattern and Cross Talk

The front view in Figure 9 shows that each element has a weakly radiating region at the bottom. This is because a $1.5\,\text{mm} \times 1\,\text{mm}$ area was left unmatched to allow a common ground lead to be terminated to the front electrode. This resulted in poor ultrasound transmission from this region, which is likely the reason for the smaller effective elevation height. The width of the radiation pattern varies along the length of the element, which is due to non-uniform coverage caused by a burr on the stencil. Additional lateral non-uniformity in the radiation pattern may be introduced by deformation due to surface tension at the edges of the matching layer during curing. To address these factors in future work, the stencil slots will be enlarged and a slightly thicker matching layer will be deposited and lapped down to size after curing.
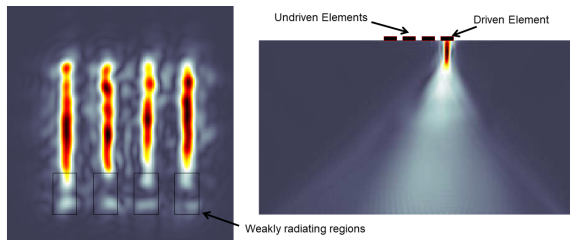

Figure 9: Left: Maximum source pressure showing the radiation pattern of the elements. A weakly radiating region can be seen at the bottom of each element. Right: Maximum pressure in the scan plane of the elements, showing that the undriven elements do not radiate when a single element is driven in isolation.

The pressure fields shown in Figure 9 show that the crosstalk between elements is negligible since none of the non-driven elements are radiating, indicating that there is no electrical interaction between elements, and that there is no acoustic interaction between elements through their common backing layer.

4.4 Pulse Echo Behaviour

To assess whether there were any internal reverberations in the transducers, they were placed in a tank of deionised water facing the wall of the tank, connected to the Vantage-256 (Verasonics), and driven with a 3 cycle tri-state pulse at a frequency of 2 MHz and an amplitude of 30 V. In this setup the tank wall acts as a reflective target. A representative time series is shown in Figure 10, which features a high amplitude burst from electrical pickup, followed by a low amplitude reflection, followed by two high amplitude reflections. The high amplitude reflections are known to arrive from the front and back of the tank wall, because as the distance between the transducer and the target is increased, the arrival times of these pulses increase. The low amplitude pulse was stationary in time when the transducer was moved, indicating that there may be internal reverberations within the transducer. The sound speed of the backing layer was measured to be $c = 1407$ m.s^{-1} and the distance of one round trip within the backing layer is $d = 2 \times 12$ mm $= 0.024$ m. Using this data would result in a pulse arrival time of $\delta t = 0.024/1407 = 17.1$ μs, and the actual pulse arrival time from Figure 10 is 18.5 μs. Allowing for the uncertainty in the backing layer thickness and sound speed, this suggests that the low amplitude reflection is from the backing-Aptflex boundary at the rear face of the backing layer.
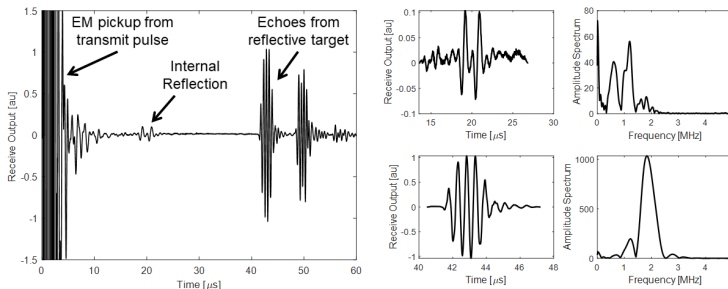

Figure 10: Left: Pulse-echo signal showing electrical pickup up until 10 μs, a low amplitude reflection from the rear face of the backing layer at 18.5 μs, and two high amplitude reflections from the front and rear face of the tank wall at 42 μs. Middle: Extracted time series for the internal reflection (top) and echoes from reflective target (bottom). Right: Amplitude spectrum for the internal reflection (top) and echoes from reflective target (bottom).

The internally reflected pulse and the first pulse to arrive from the external target were both extracted and windowed before applying a Fourier transform. Figure 10 shows that the amplitude spectrum of the internally reflected pulse contains most of its energy up to 1.2 MHz, whereas the amplitude spectrum of the pulse arriving from the external reflective target contains most of its energy at the transducer resonance frequency of 2 MHz. High frequencies are attenuated more strongly when propagating through absorbing media like tungsten-epoxy composites, so it is to be expected that the internally reflected pulse would contain most of its energy at these lower frequencies.

The internal reflections within the prototype transducers are a problem for UCT, since an incoming acoustic pulse will have an initial arrival time when it first reaches the PZT, but will have a second arrival time when it propagates past the PZT, reflects from the rear face of the backing and returns to the PZT. If the second arrival has a high enough amplitude, this could present an artefact during the image reconstruction.

5 Conclusions and Future Work

In this work, the first FlexUCT prototypes have been assembled and evaluated. Novel low-cost methods to deposit matching layers with a repeatable thickness and align PZT elements during manufacture were used to build robust, functioning 4-element transducers, which required no special equipment other than a mill, 3D-printer, and standard workshop equipment. In future, the elevation beamwidth of the transducers will be reduced by increasing their effective elevation height with a better strategy for making electrical connections to the front face of the elements, and internal reverberations in the transducers will be addressed by increasing the absorption of the backing layer. In the future, the release of an open-source design framework for a low-cost benchtop UCT system will enable more research into the optimal configuration for acquiring the minimum amount of data needed for fast, accurate UCT.

6 Acknowledgements

References

[1] C. Li, N. Duric, and L. Huang, "Clinical breast imaging using sound-speed reconstructions of ultrasound tomography data," in *Medical Imaging 2008: Ultrasonic Imaging and Signal Processing*, vol. 6920, p. 692009, International Society for Optics and Photonics, 2008.

[2] N. Duric, P. Littrup, C. Li, O. Roy, S. Schmidt, R. Janer, X. Cheng, J. Goll, O. Rama, L. Bey-Knight, *et al.*, "Breast ultrasound tomography: bridging the gap to clinical practice," in *Medical Imaging 2012: Ultrasonic Imaging, Tomography, and Therapy*, vol. 8320, p. 83200O, International Society for Optics and Photonics, 2012.

[3] N. V. Ruiter, G. Göbel, L. Berger, M. Zapf, and H. Gemmeke, "Realization of an optimized 3d usct," in *Medical Imaging 2011: Ultrasonic Imaging, Tomography, and Therapy*, vol. 7968, p. 796805, International Society for Optics and Photonics, 2011.

[4] J. Camacho, J. F. Cruza, N. González-Salido, C. Fritsch, M. Pérez-Liva, J. Herraiz, and J. Udías, "A multi-modal ultrasound breast imaging system," in *Proceedings of the International Workshop on Medical Ultrasound Tomography: 1.- 3. Nov. 2017, Speyer, Germany*, pp. 119–130, KIT Scientific Publishing, 2018.

[5] N. Duric, P. Littrup, L. Poulo, A. Babkin, R. Pevzner, E. Holsapple, O. Rama, and C. Glide, "Detection of breast cancer with ultrasound tomography: First results with the computed ultrasound risk evaluation (cure) prototype," *Medical physics*, vol. 34, no. 2, pp. 773–785, 2007.

[6] E. Boni, C. Alfred, S. Freear, J. A. Jensen, and P. Tortoli, "Ultrasound open platforms for next-generation imaging technique development," *IEEE transactions on ultrasonics, ferroelectrics, and frequency control*, vol. 65, no. 7, pp. 1078–1092, 2018.

[7] J. M. Boone, N. Shah, and T. R. Nelson, "A comprehensive analysis of DgNCTco-efficients for pendant-geometry cone-beam breast computed tomography," *Medical Physics*, vol. 31, no. 2, pp. 226–235, 2004.

[8] T. L. Szabo, *Diagnostic Ultrasound Imaging: Inside Out*. Academic Press series in biomedical engineering, Elsevier Science, 2004.

[9] F. J. Fahy, *Foundations of Engineering Acoustics*. Elsevier Science, 2000.

[10] American Piezo Ceramics, "Physical and Piezoelectric Properties of APC Materials."

[11] B. E. Treeby, J. Budisky, E. S. Wise, J. Jaros, and B. T. Cox, "Rapid calculation of acoustic fields from arbitrary continuous-wave sources," *The Journal of the Acoustical Society of America*, vol. 143, no. 1, pp. 529–537, 2018.

[12] B. E. Treeby and B. T. Cox, "k-Wave: MATLAB toolbox for the simulation and reconstruction of photoacoustic wave fields," *Journal of Biomedical Optics*, vol. 15, no. 2, p. 021314, 2010.

[13] Haifeng Wang, T. Ritter, Wenwu Cao, and K. K. Shung, "High frequency properties of passive materials for ultrasonic transducers," *IEEE Transactions on Ultrasonics, Ferroelectrics, and Frequency Control*, vol. 48, pp. 78–84, jan 2001.

[14] M. G. Grewe, T. R. Gururaja, T. R. Shrout, and R. E. Newnham, "Acoustic Properties of Particle/Polymer Composites for Ultrasonic Transducer Backing Applications," *IEEE Transactions on Ultrasonics, Ferroelectrics, and Frequency Control*, vol. 37, no. 6, pp. 506–514, 1990.

[15] B. Zeqiri, W. Scholl, and S. P. Robinson, "Measurement and testing of the acoustic properties of materials: A review," *Metrologia*, vol. 47, no. 2, 2010.

[16] S. W. Hughes, "Archimedes revisited: A faster, better, cheaper method of accurately measuring the volume of small objects," *Physics Education*, vol. 40, no. 5, pp. 468–474, 2005.

[17] A. Devaney and H. Levine, "Effective elastic parameters of random composites," *Applied Physics Letters*, vol. 37, no. 4, pp. 377–379, 1980.

[18] Y. Kim, A. D. Maxwell, T. L. Hall, Z. Xu, K. Lin, and C. A. Cain, "Rapid prototyping fabrication of focused ultrasound transducers," *IEEE Transactions on Ultrasonics, Ferroelectrics, and Frequency Control*, vol. 61, pp. 1559–1574, Sep. 2014.

[19] J. R. Morris and T. Wojcik, "Stencil printing of solder paste for fine-pitch surface mount assembly," *IEEE transactions on components, hybrids, and manufacturing technology*, vol. 14, no. 3, pp. 560–566, 1991.

[20] C. K. Aidun and N. G. Triantafillopoulos, *High-Speed Blade Coating*, pp. 637–672. Dordrecht: Springer Netherlands, 1997.

[21] N. V. Ruiter, M. Zapf, T. Hopp, R. Dapp, and H. Gemmeke, "Optimization of the aperture and the transducer characteristics of a 3d ultrasound computer tomography system," in *Medical Imaging 2014: Ultrasonic Imaging and Tomography*, vol. 9040, p. 90400U, International Society for Optics and Photonics, 2014.

[22] C. E. Baumgartner, D. M. Mills, R. S. Lewandowski, L. S. Smith, and D. G. Wildes, "Backing material for micromachined ultrasonic transducer devices," 2004.

[23] X. Zeng and R. J. McGough, "Evaluation of the angular spectrum approach for simulations of near-field pressures," *The Journal of the Acoustical Society of America*, vol. 123, no. 1, pp. 68–76, 2008.